communications materials

A Nature Portfolio journal

Article

https://doi.org/10.1038/s43246-025-00768-5

Metal-like ductility and high hardness in nitrogen-rich HfN thin films by point defect superstructuring

Marcus Lorentzon[1] ✉, Davide G. Sangiovanni[2], Naoki Takata[3], Tianqi Zhu[3], Rainer Hahn[4], Justinas Palisaitis[1], Lars Hultman[1,5], Jens Birch[1] & Naureen Ghafoor[1] ✉

The strength of refractory ceramics is much limited by their brittleness. Counterintuitively, we observe simultaneous high hardness and metallic-like ductility in highly overstoichiometric single-crystal $HfN_{1.22}$ and $HfN_{1.33}$ films grown by ion-assisted reactive magnetron sputtering. Here, we show by electron microscopy, diffraction methods, and ab-initio calculations the existence of a superstructure ordering of metal vacancies and nitrogen interstitials into sub-nanometer hyper-overstoichiometric and quasi-stoichiometric domains that self-organize into a checkerboard pattern superimposed onto the NaCl-structured lattice. A high intrinsic dislocation density and low dislocation nucleation barrier on {111} < 011> slip systems enable extraordinary ductility and strain hardening at >50% strain, in room temperature uniaxial compression of $HfN_{1.22}$ micropillars. The films simultaneously exhibit a high hardness – tunable up to 28 GPa via control of stoichiometry – and a remarkable fracture resistance due to dislocation-mediated stress dissipation. The presented findings provide a route for synthesizing nitride superstructured films with unique hardness/toughness combinations.

The physical and chemical properties of ceramics provide engineering opportunities in various applications. Ceramics vary widely in hardness, some relatively soft and others exceptionally hard. However, due to high bond strength with associated low dislocation activity, inherent brittleness and poor fracture toughness is a common problem that severely limits their use[1]. The issue of brittleness in ceramics has traditionally been addressed by using structural nanoengineering and extrinsic toughening[2,3] where enhanced toughness can be obtained primarily through crack deflection, crack bridging, transformation toughening, and interfacial sliding.

More recently, there has been evidence of intrinsic plasticity in metal oxides through the facilitation of dislocation activity by structure design, provided that abundant dislocations can be introduced into the material. For example, a dislocation density of over $10^{14}\,m^{-2}$ introduced through polishing, $SrTiO_3$ demonstrated plastic ductility and nearly doubled its fracture toughness[4], and introducing dislocations by pre-loading, upon annealing above the brittle-to-ductile transition temperature, room-temperature ductility was observed in TiO_2 and Al_2O_3[5]. Moreover, plasticity in La_2O_3 and CeO_2 was achieved by engineering coherent interfaces with metal inclusions, which allowed for the nucleation of dislocations in the metal that then injected into the ceramics[6]. These results suggest that plasticity in ceramics is hindered not by dislocation mobility, but by a resistance to dislocation nucleation.

Here, we seek to synthesize dislocation-rich nitride ceramics in their as-deposited state. Refractory transition metal (TM) nitrides are an industrially important class of ceramics, often employed as functional thin films and coatings with applications in high-temperature and pressure environments like cutting tools, microelectronics, fuel cells, and battery technology[7,8]. Over the last thirty years, there has been significant progress in developing TM-nitride hard coatings, evolving from binary to ternary and multi-component compositions. For example, alloying TiN with isostructural cubic-phase AlN provides for hardening and increased thermal stability, oxidation, and wear resistance of the coating, thus extending the tool lifetime and enabling new metal forming processes[9]. Alloying has also been used to manipulate electronic structures to improve intrinsic material ductility[10]. Yet, brittleness remains a concern in applications. Controlling the nitride film deposition parameters allows for tuning the metal/N stoichiometry by incorporation of nitrogen interstitial point defects or cation (metal) and anion (nitrogen) vacancies. Anion vacancies have been effective in enhancing the hardness, plasticity, and toughness of VN_y[11],

[1]Thin Film Physics Division, Department of Physics, Chemistry and Biology (IFM), Linköping University, SE-58183 Linköping, Sweden. [2]Theoretical Physics Division, Department of Physics, Chemistry and Biology (IFM), Linköping University, SE-58183 Linköping, Sweden. [3]Department of Materials Design Innovation Engineering, Graduate School of Engineering, Nagoya University, Nagoya, Japan. [4]Christian Doppler Laboratory for Surface Engineering of high-performance Components, TU Wien, A-1060 Wien, Austria. [5]Center for Plasma and Thin Film Technologies, Ming Chi University of Technology, 84 Gungjuan Rd., Taishan Dist, New Taipei City, 24301, Taiwan. ✉e-mail: marcus.lorentzon@liu.se; naureen.ghafoor@liu.se

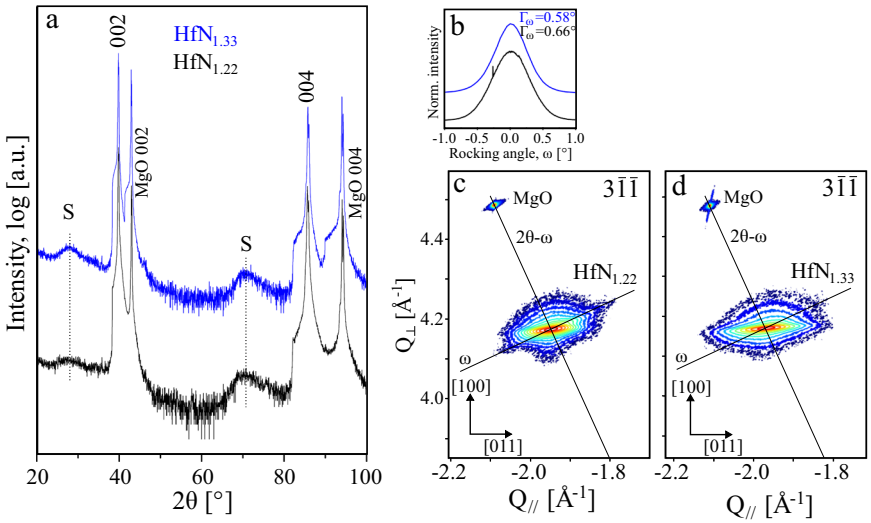

Fig. 1 | Structural characterization by x-ray diffraction. a XRD $\omega-2\theta$ scans for 2θ range: 20−100°. Two broad peaks, centered at $2\theta \approx 28°$ and $2\theta \approx 70°$, labeled "S", originates from a compositionally modulated superstructure. **b** shows normalized ω-rocking curves, centered around $\omega = 0°$, from the 200 peak and corresponding FWHM, Γ_ω values. The substrate peak gave $^{002}\Gamma_\omega = 0.013°$. The profiles in the scans are vertically offset for clarity. Additional information is discussed in Supplementary Section 2. **c**, **d** show RSM intensity (log) plots around the asymmetric $3\bar{1}\bar{1}$ peak for $HfN_{1.22}$ and $HfN_{1.33}$ respectively. The broadening in the ω-direction, most pronounced for MgO spots, is attributed to wafer curvature, but is a very limited effect. A 2θ streak, stemming from the monochromator, is seen for the MgO peak in (**d**).

$VMoN_y$[12], and WN_y/TiN superlattices[13]. Controlling the vacancy concentrations along with stoichiometry can also be exploited to selectively stabilize crystal phases that exhibit desired properties[14].

HfN is an ultra-high temperature ceramics[15] that, similar to TiN and ZrN, can withstand extreme conditions[16,17]. At variance with the well-studied TiN, overstoichiometric HfN_y thin films, with high density of lattice point defects, can be readily grown by reactive magnetron sputtering[18,19]. Previous reports show conflicting results on the effects of vacancies on hardness and elastic modulus[18,20], while plasticity has not yet been investigated. Therefore, we selected HfN_y single-crystal thin films as a model system to study the crystal and point defect structure and their impact on the toughening mechanisms.

We propose a synthesis route for high-quality epitaxial HfN_y thin films on MgO(001) substrates, with tailorable overstoichiometry accommodated by cation vacancies and N interstitials, using ion-assisted magnetron sputtering. A high dislocation density in as-deposited films was promoted via the system's significant lattice mismatch (~7.5%). A point-defect self-organization, consisting of quasi-stoichiometric and hyper-overstoichiometric nanosized domains in an ordered checkerboard superstructure, is obtained. This original microstructural feature is demonstrated by high-resolution electron microscopy, electron and x-ray diffraction, and ab initio simulations. Subsequent mechanical tests reveal a combination of high hardness, room temperature dislocation-mediated ductility, and strain hardening. A sought-for property combination in refractory ceramics is thus demonstrated.

Results and discussion

Epitaxial HfN_y single-crystal films were grown on MgO(001) substrates using ion-assisted reactive magnetron sputtering[21]. Combined results from Rutherford backscattering and time-of-flight elastic recoil detection (see Supplementary Section 1) show that HfN_y films are highly nitrogen-overstoichiometric, with $HfN_{1.22}$ and $HfN_{1.33}$. In addition, Ar and Zr contaminants were detected at 0.7 at.% Ar, 1.2 at.% Zr, and 0.5 at.% Ar, 1.5 at.% Zr, respectively. The Ar was trapped from the sputter gas, while Zr is a common contaminant in Hf targets. The increased N content is partly attributed to the reaction kinetics of nitrogen on the film surface during high temperature (800 °C) growth, in excess N_2 partial pressure. Concurrently, the growing film is subjected to low energy ion bombardment (<25 eV) of Ar^+ and N_2^+, attracted by a substrate bias of −30 V from the plasma. The nearly twice as high ion-to-metal flux ratio measured for $HfN_{1.33}$ ($J_{Ion}/J_{Me} = 28$) compared to $HfN_{1.22}$ ($J_{Ion}/J_{Me} = 15$), indicates a larger degree of metal vacancy generation or nitrogen trapping, with a higher ion flux, due to near surface collision cascades[22,23]. The films' mass density decreased from a bulk value of 13.8 g·cm^{-3} to 12.6 g·cm^{-3} for $HfN_{1.22}$ and 11.7 g·cm^{-3} for $HfN_{1.33}$.

X-ray diffraction (XRD) ω-2θ scans in Fig. 1a show high-quality epitaxial B1-NaCl structured $HfN_{1.22}$ and $HfN_{1.33}$ films, with resolved $K_{\alpha1}$-$K_{\alpha2}$ doublets of 00l film peaks, with intensities higher than that of the MgO substrate. Rocking curves in Fig. 1b shows a decreasing FWHM, $^{002}\Gamma_\omega$, from 0.66° to 0.58°, for increasing nitrogen content. Contrary to previous results where a substantially increased FWHM with nitrogen off-stoichiometry was reported, from $^{002}\Gamma_\omega = 0.58°$ for stoichiometric HfN, to $^{002}\Gamma_\omega = 0.9°$ for $HfN_{1.38}$[18]. In this case, the exceptionally increased film quality stems from the ion-assisted sputtering process, which enhances adatom diffusion to enable atoms to find a minimum energy site[21].

A notable feature observed in the XRD scans are two low-intensity broad peaks (humps), marked with "S" in Fig. 1a, with slightly higher intensity and smaller $\Gamma_{2\theta}$ for $HfN_{1.33}$. The peaks are roughly equally spaced from the 002 and 004 film peaks which, at first glance, indicates the inclusion of a secondary phase, as a previous study on HfN_y reported[18]. However, the peak positions do not match any known nitrogen-rich Hf-N phase. Instead, these reflections are attributed to a compositionally modulated superstructure, which is discussed below alongside scanning transmission electron microscopy (STEM) and selected area electron diffraction (SAED) analyses.

Reciprocal space maps (RSM) around the asymmetric $3\bar{1}\bar{1}$ reflections of the film and MgO substrate, shown in Fig. 1c, d revealed a relaxed film lattice in both cases, with $a_0 = 4.525$ Å and 4.518 Å for $HfN_{1.22}$ and $HfN_{1.33}$ respectively (see Supplementary Section 3 for calculations). A similar or slightly smaller lattice parameter compared to bulk HfN ($a_0 = 4.5253$ Å[24]) was obtained, where a decreasing a_0 with increasing over-stoichiometry is a common trend for HfN_y[18,19,25]. The lattice slightly expands by the presence of nitrogen interstitial, whereas Hf vacancies have a greater contracting effect[18]. The relatively unchanged lattice parameter compared to stoichiometric HfN, and the large over-stoichiometry of the films suggest that both interstitial N and Hf vacancies are present in the films. The asymmetric lattice points further reveal a substantial lateral broadening, a small transverse broadening and a slightly tilted reciprocal lattice point. The angle between the tilted peak and a horizontal line was $\varphi < 8.7°$, indicating that limited lateral size is the dominating effect. The lateral broadening, L, separated from the mosaic tilt, α[26], is calculated (see Supplementary Section 3) as $L = 17.7$ nm and $\alpha = 0.181°$ (652 arcseconds) for $HfN_{1.22}$, and $L = 14.3$ nm and $\alpha = 0.121°$ (434 arcseconds) for $HfN_{1.33}$. A small lateral size is often attributed to a film with thin columnar domains; however, in the present scenario, x-ray coherency in the lateral direction is interrupted by the presence of a very large density of threading dislocations as well as dislocations loops rather by the domain size, which will be discussed below.

Cross-sectional high-angle annular dark field (HAADF) STEM and SAED in Fig. 2, together with images presented in Supplementary Section 4 confirms the cube-on-cube epitaxial $HfN_{1.33}$ film on the MgO(001)

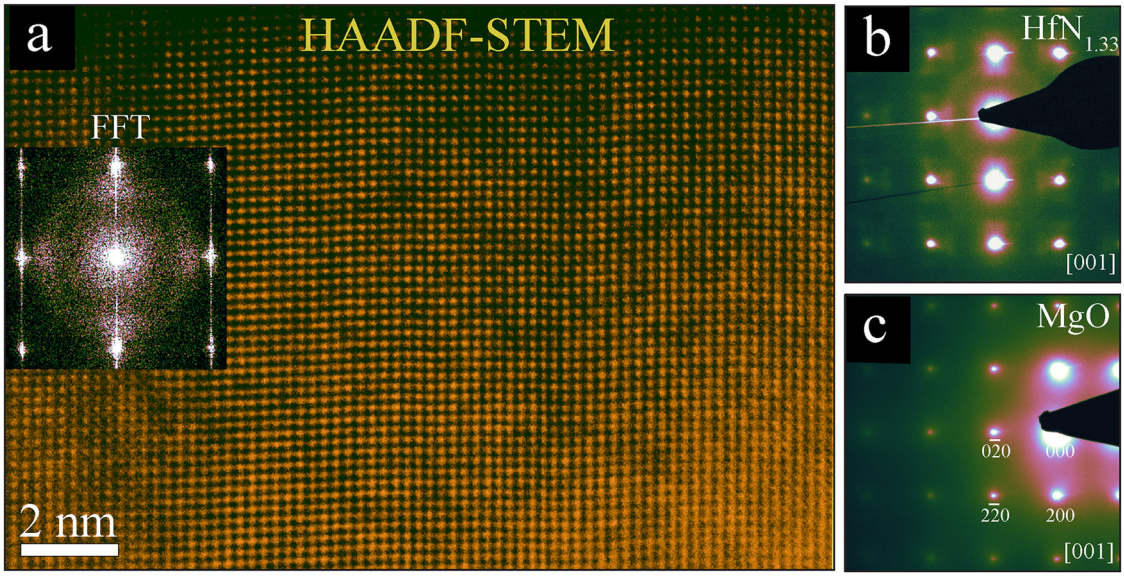

Fig. 2 | Lattice resolved HAADF STEM imaging and electron diffraction. a Color-coded cross-sectional high resolution HAADF STEM micrograph of the $HfN_{1.33}$ film recorded along the [001] zone axis and a small camera length for enhanced z-contrast. Nanometer-sized domains are seen as bright and dark areas. An FFT-inset show lobes of weak intensity from the sharp main spots. **b**, **c** Corresponding color-coded SAED patterns from the $HfN_{1.33}$ film, with satellites around each main spot, and MgO substrate, respectively. The presence of any imaging artifacts in the diffraction pattern is ruled-out upon comparing with the adjacent substrate diffraction pattern and FFT. The diffuse circular ring in (**b**), centered around the direct beam, is attributed to the damaged amorphous surface layer from ion milling.

substrate. The lattice resolved STEM micrographs also reveal nanometer-sized domains with sequential bright and dark contrasts, superimposed on the single-crystal lattice, resembling a checkerboard pattern. These domains unequivocally correspond to N-rich HfN (dark) and Hf-rich HfN (bright) domains in the binary compound, since the contrast is determined by the charge density. The corresponding single-crystal SAED pattern in Fig. 2b shows lobes of weak intensity surrounding each main diffraction peak in a quadratic manner, best observed in the left part of Fig. 2b. These satellite reflections are a clear characteristic of a 3D superstructure.

Accordingly, the identified 3D checkerboard superstructure explains the broad peaks labeled "S" in XRD in Fig. 1, as superstructure satellites. An increased nitrogen content results in more intense satellite peaks in XRD, while the peak position is maintained. The satellite position is related to the average superstructure period, $<\Lambda>$, of the checkerboard pattern, calculated using Eq. (1)[27], where n is the satellite reflection order, θ_0 is the angle of the main peak, and θ_n is the angle of the n^{th} satellite peak[27]. Thus, an equal average period for both compositions. The 002 and 004 satellite separations of $\Delta 2\theta \approx 11.9°$ and $\Delta 2\theta \approx 15.5°$, respectively, both yielded an average period of about $<\Lambda> = 7.5$ Å, where for a non-perfect ordering of nm-sized domains, only $n = 1$ can be expected.

This small period agrees well with the directly measured period in the STEM micrographs in Fig. 2. Additionally, the checkerboard pattern is aligned in the <001> directions, determined from the shape of the satellite lobes in electron diffraction and the fact that the domains are visible in STEM despite the projection of multiple domains in the comparatively thick foil. We submit that the Hf-rich domains are near-stoichiometric HfN, while the N-enriched domains, on the other hand, are hyper-overstoichiometric with accumulated Hf vacancies and interstitial N defects, as a means to reduce the system's enthalpy. Thus, the checkerboard pattern is effective in minimizing the forced additional energy condition by virtue of mutual annihilation of inhomogeneous strain fields.

$$\Lambda = \frac{n\lambda}{2\left|\sin\theta_0 - \sin\theta_n\right|} \quad (1)$$

Density functional theory (DFT) calculations, ab-initio molecular dynamics (AIMD) and Monte Carlo (MC) simulations based on the machine-learning-interatomic potential (MLIP) trained during AIMD (see Supplementary Section 5) are employed to understand energetic mechanisms leading to defect superstructuring in $HfN_{1.22}$ thin films. The propensity of HfN at incorporating cation vacancies and N interstitials is assessed by comparison with defect formation energies separately evaluated by DFT for TiN, due to the strong preference of TiN towards N-depletion[28]. Results in Table 1 indicate that cation vacancies (V_{me}) and N self-interstitials (N_{SI}) are more stable in Hf_xN compared to Ti_xN. In both nitrides, metal vacancies repel each other, consistent with previous results[29,30], However, introducing nitrogen antisite (N_{AS}) defects together with metal vacancies reveals different behavior of Hf_xN_y versus Ti_xN_y. A single antisite defect in Hf_xN_y has nearly 3 eV lower formation energy (8.72 vs 11.67 eV) compared to Ti_xN_y, which is a first indication that HfN can accommodate overstoichiometry by combining excess N with metal depletion. A further addition of metal vacancies near N_{AS} defects results in a substantial reduction of the total defect formation energy in Hf_xN_y. These results indicate that clustering of metal vacancies and nitrogen interstitials is less unfavorable in HfN.

The relatively high point defect formation energy calculated for both material systems suggests that a substantial concentration of N interstitials and cation vacancies can only be achieved in synthesis conditions far from thermodynamic equilibrium. The reactive magnetron sputtering conditions used in this work, with a growth temperature of 800 °C, satisfies this condition, with a homologous temperature of $T_{growth} / T_{melt} = 0.3$ ($T_{melt} = 3300$ °C). In addition, the continuous high flux of low energy ion bombardment introduces kinetic effects, where metal vacancies can form, and subsequently buried, through energetic collision cascades at and just below the surface of the growing film. Similarly, bombarding nitrogen ions may be trapped in interstitial positions or even in vacant cation sites.

The defect structure of $HfN_{1.22}$ predicted by annealing/cooling cycles in AIMD (Fig. 3a) shows a striking resemblance with experimental results from STEM, SAED and XRD, confirming the hypothesis of quasi-stoichiometric and hyper-overstoichiometric domains in a checkerboard superstructure aligned in the <001> directions. The calculations yield a cubic lattice parameter of 4.56 ± 0.03 Å which, combined with the N/Hf composition (119/98 = 1.214), corresponds to a mass density of 12.4 ± 0.1 g·cm^{-3}, in very good agreement with experimental results. The size of the domains is slightly overestimated in the calculations, with a checkerboard period of approximately 13.5 Å, while experiments show a period of 7.5 Å. The discrepancy may be due to the constraint imposed by the periodic

boundary conditions of supercell calculations and by partial incommensurability of the supercell size with experimentally determined period.

We use MLIP-MC sampling for rapidly screening the energy of different defect arrangements in $HfN_{1.22}$. The differences in energy (ΔE) from the most stable configuration correlate with a structural descriptor (Fig. 3e). The latter considers the spatial width of V_{me} distributions together with V_{me}/N_{SI} distances. Thus, the structural descriptor serves verifying whether defect-clustering in $HfN_{1.22}$ arises from energetic effects. As shown by Fig. 3a–d (with corresponding ΔE), defect clustering is unequivocally favored over a disordered random defect distribution. Combined with information from Table 1, we infer that cation vacancies tend to cluster only because of the simultaneous presence of N self-interstitials. The checkerboard superstructure, illustrated in Fig. 3f, has a great influence on the mechanical properties of $HfN_{1.22}$, as discussed below, where the organized defects aid dislocation-mediated plasticity. It is worth noting that some defect configurations resemble those identified by DFT for metal-deficient TiC[31], suggesting that defect structures similar to Hf_xN_y could be realized in other carbonitrides.

Color-coded HAADF STEM micrographs in Fig. 4a–c reveal a dense dislocation structure in the as-grown $HfN_{1.22}$ film. These threading dislocations form early in the growth process due to imperfections on the substrate surface as well as the large lattice mismatch and extend over the full thickness of the film. The threading dislocation density is ~10^{10} cm^{-2}, approximated from the STEM images. However, the majority of the 7.5%

Table 1 | Point defect formation energies calculated by DFT for Hf_xN_y and Ti_xN_y

Supercell	Composition	N/TM ratio	HfN defect formation energy (eV)	TiN defect formation energy (eV)
Defect-free	$TM_{1.00}N_{1.00}$	1.00	–	–
$V_{me\ (metal)}$	$TM_{0.99}N_{1.00}$	1.01	1.32	3.20
$2V_{me}$ (isolated)	$TM_{0.98}N_{1.00}$	1.02	2.68	6.42
$2V_{me}$ (1st neighb.)	$TM_{0.98}N_{1.00}$	1.02	3.62	7.18
$2V_{me}$ (2nd neighb.)	$TM_{0.98}N_{1.00}$	1.02	3.10	–
$2V_{me}$ (3rd neighb.)	$TM_{0.98}N_{1.00}$	1.02	2.90	–
$3V_{me}$ (isolated)	$TM_{0.97}N_{1.00}$	1.03	4.54	9.92
$3V_{me}$ (1st neighb.)	$TM_{0.97}N_{1.00}$	1.03	6.30	11.44
$N_{AS\ (antisite)}$	$TM_{0.99}N_{1.01}$	1.02	8.72	11.67
$N_{AS} + V_{me}$	$TM_{0.98}N_{1.01}$	1.03	7.95	11.29
$N_{AS} + 2V_{me}$	$TM_{0.97}N_{1.01}$	1.04	7.28	13.68
$N_{AS} + 3V_{me}$	$TM_{0.96}N_{1.01}$	1.05	9.64	17.90
N_{SI} [110] dumbbell	$TM_{1.00}N_{1.01}$	1.01	3.84	4.84
N_{SI} cell-center	$TM_{1.00}N_{1.01}$	1.01	3.13	5.78

V_{me} cation vacancy, N_{AS} = N antisite, i.e., a N atom replaces a metal atom in cation position, N_{SI} N self-interstitial bonded along [110] to a N lattice atom (dumbbell) or located at the center of a cubic unit cell.

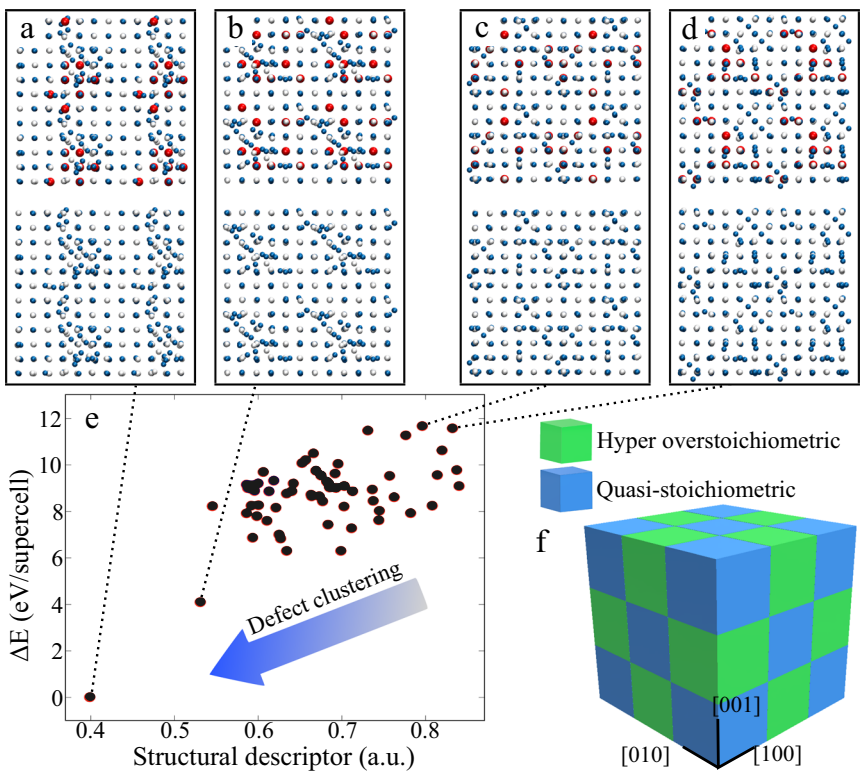

Fig. 3 | Superstructure validation by calculations. **a**–**d** Selected defect structures in $Hf_{0.91}N_{1.10}$ supercells with stochastic defect arrangements, mimicking $HfN_{1.22}$ composition. **e** MLIP energies of a wide range of structures including the ones in (**a**–**d**). All supercells contain the same number of Hf^{98} and N (119) atoms on a 3 × 3 × 3 B1 lattice, and the snapshot is taken in the [001] zone axis. Note that the snapshots display four $Hf_{0.91}N_{1.10}$ supercell replicas. The two lowest-energy structures (**a**) and (**b**) are characterized by local agglomerations of cation vacancies (red spheres in upper part of supercell snapshots) decorated by N self-interstitials (blue spheres). Conversely, high-energy structures in (**c**) and (**d**) show a rather homogeneous distribution of defects over the entire supercell volume. A good reliability of the MLIP results was confirmed by re-relaxing the structures in (**a**–**d**) by DFT calculations (see Supplementary Section 5). f) Schematic of the 3-dimensional checkerboard superstructure with main <100> axes relating to the B1 NaCl lattice.

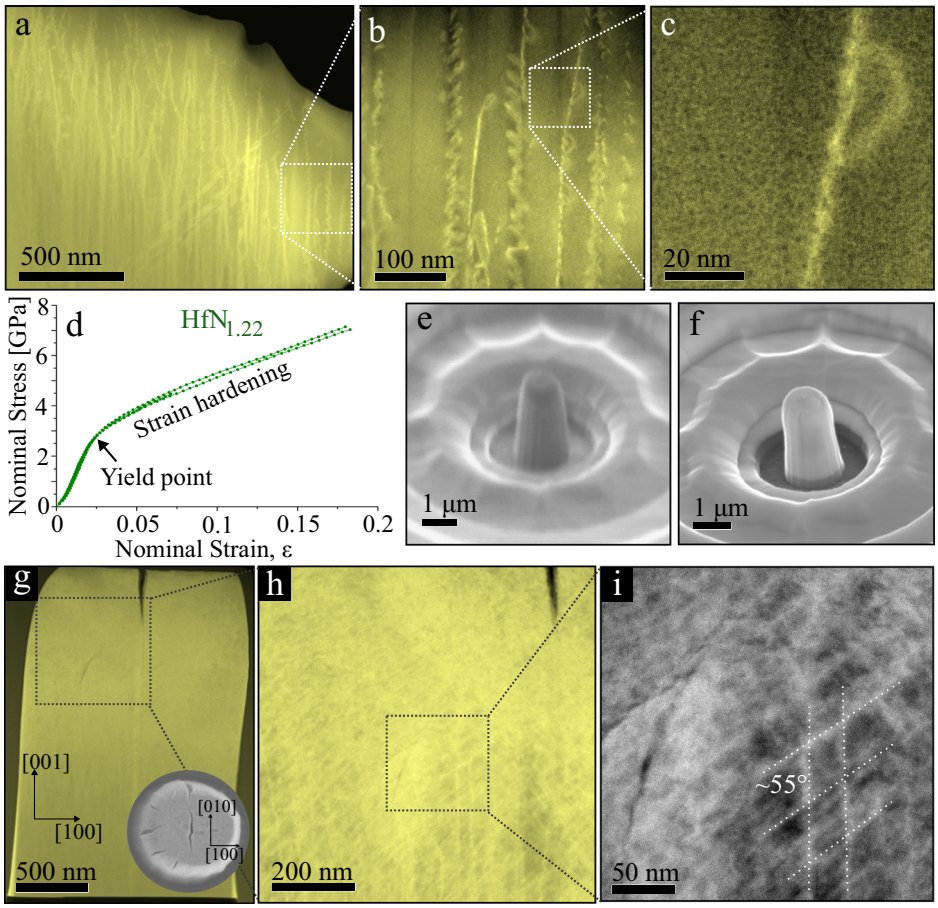

Fig. 4 | Dislocation structures and micropillar compression testing of the $HfN_{1.22}$ film. a–c Color-coded cross-sectional high-resolution HAADF STEM images in the [001] zone axis, highlighting dislocations. **c** Threading dislocation with a dislocation loop extension, in which the speckled contrast corresponds to the compositionally modulated superstructure. **d** Three stress-strain curves from milled micropillars during compression testing. **e**, **f** Representative SEM micrographs of as-milled and post-mortem pillars, respectively. In-depth post-mortem analysis was done using a lamella taken from the pillar in (**f**) by focused ion beam lift-out. **g–i** HAADF STEM micrographs in the [010] zone-axis. The overview micrograph in (**g**) shows that substantial mass-transport has taken place in the top half of the pillar. The inset is a top-view SEM micrograph with markings of the crystal directions. The high dislocation density in (**h**) and marked dislocations in (**i**) show an average dislocation tilt of approximately 55° with respect to the sample normal. A ~ 400 nm long surface crack and a ~ 200 nm long crack in the bulk of the pillar were effectively stopped without catastrophic fracture. Supplementary Fig. S9 in Supplementary Section 6 show arcs in SAED patterns of the pillar in g) which give further evidence of ductility.

lattice mismatch between MgO and HfN is relieved by misfit dislocations at the film-substrate interface.

Most threading dislocations are, in addition, associated with multiple tightly spaced dislocation loops that fan out by 10–20 nm, attached to a vertical threading dislocation, suggesting that the threading dislocation lower the nucleation barrier for dislocation loop formation. The checkerboard point defect structure in the present HfN_y films (speckled contrast in Fig. 4c) is disturbed in the presence of the threading dislocations which therefore may cause point defects diffusion and accumulation, ultimately condensing into a dislocation loop nucleus. Thus, we believe that the cause of the dislocation loops is due to a rearrangement of the Hf-vacancies in close proximity to the threading dislocation. An accumulation of vacancies increases the local strain which may cause additional Hf-vacancy diffusion, resulting in a loop expansion. The local strain will, however, decrease with an increasing loop radius as the lattice distortion is spread over a larger area. Thus, a relatively uniform dislocation loop size is obtained as the driving force for expansion is reduced below the critical point required for vacancy diffusion. The N-interstitial point defects are not expected to generate dislocations loops as the relatively small N atom can be more easily accommodated in the lattice.

Similarly, isolated dislocation loops has been found in ion-assisted magnetron sputtered TiN single crystal thin films, where the density of dislocation loops increased with the number of point defects created during growth, in turn affected by both growth temperature and ion energy[22]. The apparently substantially reduced nucleation barrier for new dislocations in the present HfN_y film as caused by the high point defect density, in particular Hf-vacancies, is encouraging for an improved plasticity of the material, more akin to the behavior of ductile metals than brittle ceramics.

The $HfN_{1.22}$ and for $HfN_{1.33}$ films both qualify for hard coatings with a nanoindentation hardness of 26.0 ± 2.3 GPa and 27.7 ± 0.9 GPa, respectively, similar to reports for HfN_y[25,32], and HfAlN[33] films. Seo et al. also observed a substantial increase in hardness upon deviation from stoichiometric HfN_y films, where H = 32 GPa was found for $HfN_{1.32}$[18]. They attributed the hardness increase to dislocation pinning at Hf-vacancies and N-interstitials, increasing the resistance to dislocation glide. With a similar argument, we instead attribute the increase of hardness to the checkerboard superstructure, with ordering of point defects along <001>, where the more pronounced checkerboard pattern in $HfN_{1.33}$, are more effective at pinning.

Figure 4d shows the stress-strain curves of uniaxially compressed micropillars milled from the $HfN_{1.22}$ film. All three compressed pillars deform consistently with a small scatter in the stress-strain curves and a notably high level of ductility. The yield point occurred at a nominal stress of ~2.6 GPa at a plastic strain of ~2%, followed by ductile deformation and significant strain hardening of the material. None of the pillars failed catastrophically and the loading was stopped after a nominal strain of 7% and 15%. The maximum recorded stress was more than 7 GPa due to strain hardening, nearly triple the yield strength, while the ultimate strength was not reached. Representative scanning electron microscopy (SEM) micrographs of the pillars pre- and post-mortem, and a post-mortem HAADF STEM overview in Fig. 4e–g show that the top-half of the pillar underwent ductile plastic deformation. The behavior of such global plasticity is rare for hard transition metal nitrides but resembles ductile metals with large dislocation mediated mass transport. Typically, complete brittle fracture or localized massive slip just past the elastic region appears in micropillar compression tests of close-to-stoichiometric transition-metal nitride and carbide hard coatings[34–39].

The pillar plastic deformation and strain hardening are further examined through high-resolution HAADF STEM imaging in Fig. 4g–i. The brighter contrast in the top half of the pillar stems from an increased dislocation density compared to the as-grown film. A dense dislocation network has evolved (Fig. 4h), which makes for a ductile work hardening mechanism associated with metals, where the dislocation network inhibits further dislocation movement and multiplication[40]. On average, two distinct

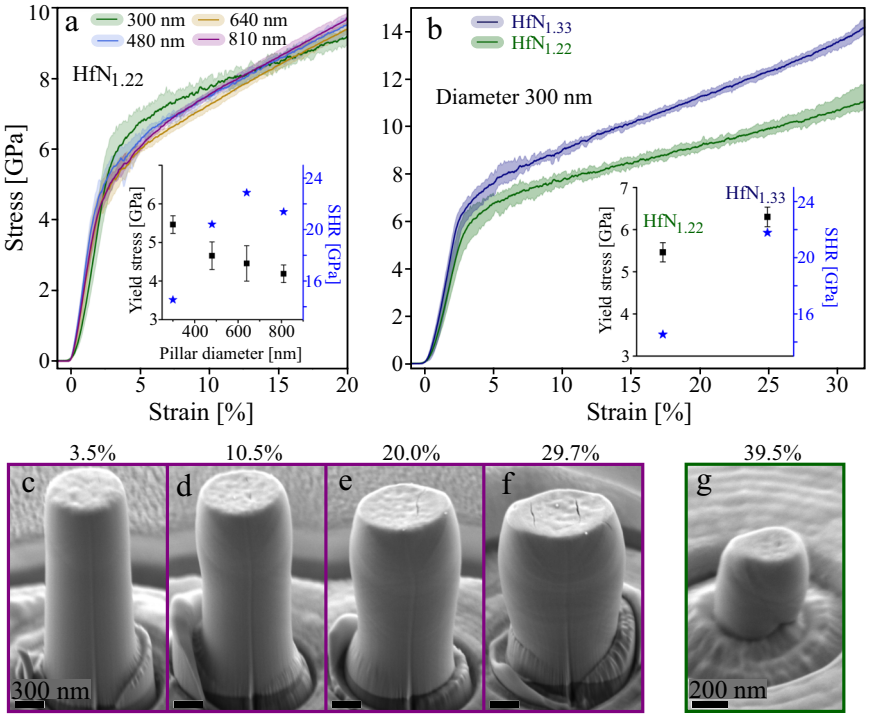

Fig. 5 | Micropillar compression testing and size-effects. a Average engineering stress-strain curves for compression of $HfN_{1.22}$ pillars with different sizes to evaluate size effects. **b** Average engineering stress-strain curves for compression of 300 diameter pillars of $HfN_{1.22}$ and $HfN_{1.33}$, respectively. The insets in (**a**, **b**) show the yield stress and the strain hardening rate, SHR. The error (max, min) is given by the colored areas around the average line. **c–f** SEM micrographs of 810 nm diameter $HfN_{1.22}$ pillars compressed to different amounts of strain, up to ~30%. **g** SEM micrograph of a 300 nm diameter $HfN_{1.22}$ pillar compressed to ~40% strain, exhibiting a different plastic deformation. More details on stress-strain curves and SEM micrographs are presented in Supplementary Section 6.

directions of the dislocations can be observed: as-grown vertical threading dislocations in [001], and others with a ~ 55° angle to the vertical. The vertical dislocations appear sessile as the number density correspond rather well with the intrinsic threading dislocation density. However, no sign of the intrinsic dislocation loops can be found in the compressed pillar, indicating that these loops have moved and expanded through the lattice, which can partly explain the remarkable plasticity. The substantially increased dislocation density also suggests nucleation of additional dislocations. Given the tilt angle of ~55° with respect to [001] and previous report of preferred slip system in HfN[41], we assign these nucleated dislocations to the {111} < 110> slip system. The enhanced ductility can thus be explained by motion of dislocation loops and a low barrier for dislocation nucleation. Both of which are attributed to the large number of point defects in the lattice, in particular Hf-vacancies, as discussed above.

An additional series of 28 pillars with diameters of 810 nm, 640 nm, 480 nm, and 300 nm were milled from the $HfN_{1.22}$ film to assess potential size effects of the plastic response. Moreover, the plastic response of $HfN_{1.33}$ was evaluated using 7 pillars of 300 nm diameter. The resulting engineering stress-strain curves are presented in Fig. 5a, b. Despite up to 50% strain, not a single pillar failed catastrophically, showing an extraordinary malleability. SEM micrographs of compressed $HfN_{1.22}$ pillars (810 nm) are shown in Fig. 5c–f, representative for all of the compression tests except for 300 nm diameter $HfN_{1.22}$ pillars, see Fig. 5g, which tend to deform differently. A remarkable agreement in the stress-strain curves was obtained for the three larger sized $HfN_{1.22}$ pillars. A larger disagreement was found for the smallest diameter, 300 nm, where the yield stress substantially increased and the flow stress, i.e. strain hardening rate, SHR, substantially decreased, indicating an onset of significant size-effects. Although calculating SHR from engineering stress-strain curves is not recommended, it gives a reasonable indication of the true value and enables a comparison between the samples in this study. The yield stress and strain hardening rates are plotted in the inset of Fig. 5a, which clearly shows the deviation, and is attributed to a change of the deformation mechanism. The 300 nm diameter $HfN_{1.22}$ pillars, in addition to the uniform plastic deformation with material being symmetrically squeezed out, also exhibited pronounced shearing at 39.5% strain, and even some fracture or slip at >50% strain. This change may be related to the mechanical annealing effect which becomes stronger at smaller pillar sizes[42]. For larger pillars, the yield stress increased slightly with decreasing size.

The pillar taper and diameter selection can significantly affect the calculated stress-strain curves and the yield and flow stresses[43]. As seen in Fig. 5c–f, the plastic deformation starts at the top of the pillar and progressively grows downwards at increasing strains. For accurate yield stress measurement, the top diameter is used for stress-strain calculations from the load-displacement data. However, a consequence of the non-zero taper is an increased flow stress during plastic deformation, due to the gradually increasing cross-sectional area of the plastically deformed zone. This effect, estimated by analyzing the plastically deformed zone at different strains from the SEM micrographs (see Fig. 5 and Supplementary Section 6, Supplementary Figs. S10–S14) and considering the ~2° taper, contributes up to 6.6 GPa of the SHR for 810 nm pillars. Thus, up to 30% of the SHR is caused by the taper, while more than ~70% is attributed to real strain hardening effects from interacting dislocations, as discussed above. The mechanical response from Fig. 4d agrees qualitatively very well with the results in Fig. 5a: No catastrophic failure and substantial strain hardening. However, differences in test parameters—like the ~4.5° taper and mid-point diameter – fully explains the lower yield stress and larger SHR in Fig. 4d. Therefore, the results in Fig. 5 are considered more accurate.

The comparison of the stress-strain curves between 300 nm pillars of $HfN_{1.22}$ and $HfN_{1.33}$ in Fig. 5b, shows that $HfN_{1.33}$'s higher over-stoichiometry improves the mechanical performance. A substantially increased yield stress (6.3 ± 0.23 GPa), compared to $HfN_{1.22}$ (5.5 ± 0.23 GPa) was obtained, and a similar SHR to the larger $HfN_{1.22}$ pillars. Together with uniform plastic deformation of the $HfN_{1.33}$ pillars, (see Supplementary Section 6, Supplementary Fig. S14) suggests minimal size effects for $HfN_{1.33}$. The higher yield strength of $HfN_{1.33}$ correlates well with its higher hardness, attributed to more effective dislocation pinning by the more pronounced checkerboard superstructure. Thus, a larger over-stoichiometry from an increased number of Hf-vacancies and N-interstitials results in a stronger material that simultaneously allows for effective dislocation generation, even at very small dimensions.

B1 NaCl-structured transition metal nitrides and carbides have dislocation Burgers vector along the close-packed <110> directions and glide-planes on {111}, {110} or {001}. Recent experiments evidenced the presence of {001}<110>, {110}<110>, and {111}<110> edge dislocations in as-deposited epitaxial TiN films[44]. Nevertheless, different dislocations may present substantial differences in core energy and Peierls stress, where both

are affected by the local stoichiometry. The primarily activated plane is determined by the orientation of the load in relation to the crystal axes and by the energy required for dislocation nucleation and/or motion on respective plane. Many hard coating materials prefer to slip on the {110} planes at room temperature[38,39,45–50], For TiN, nearly twice the critical stress is required to nucleate a dislocation on {111} compared to {110} planes[49].

The Schmid factors in the present experiment with compression in [001] and slip in <110> directions are calculated for different planes: 0 for {001}, 0.5 for {110}, and 0.408 for {111}. The critical resolved stress is thus highest in the {110}<110> slip system, however as noted above, different material systems can prefer certain slip systems over others, where $HfN_{1.22}$ instead prefer the {111}<110> slip system. This may enable an enhanced ductility because of twice as many slip systems compared to {110}<110> and considering the geometry of the compression experiment. However, the exceptional room-temperature ductility of $HfN_{1.22}$ and $HfN_{1.33}$ cannot be explained solely by a different preferred slip system. Instead, the large threading dislocation density of $10^{14}\,m^{-2}$, and particularly the even more abundant dislocation loops (Fig. 4b) play an active role in the plastic response by dislocation motion. Furthermore, the nucleation of new dislocations can continue by rearrangement of remaining vacancies due to the externally applied strain in the same way discussed previously, thus enabling an enhanced ductility. Similar metal-like behavior of room temperature brittle oxide ceramics has been reported in several cases after introducing a sufficiently high dislocation density[4–6], It should, however, be noted that plasticity in brittle ceramics is common at elevated temperatures[51,52], including HfN at 2300 °C[41].

The SEM micrographs in Fig. 5e–f and the STEM analysis of the post-mortem $HfN_{1.22}$ pillar in Fig. 4g–i reveal an improved fracture toughness by the effectively stopped vertical surface crack after ~400 nm, that initiated on the (010) plane, where {001} are common cleavage planes in transition metal nitrides due to their lowest surface energy[53]. Furthermore, a small crack within the pillar, Fig. 4i, ~200 nm long, was also stopped in its path. The toughening mechanism could be crack tip blunting due to dislocation emission near the tip[54], enabled by the apparent low dislocation nucleation barrier.

Conclusions

Single-crystal $HfN_{1.22}$ and $HfN_{1.33}$ films with a compositionally modulated superstructure were grown by ion-assisted reactive magnetron sputter epitaxy on MgO(001) substrates. The superstructure exhibits checkerboard structure along <001> directions, with a period of about 7.5 Å. It forms during film synthesis by excess N segregating to hyper-overstoichiometric domains with agglomerated Hf-vacancies and N interstitials, together with domains of quasi-stoichiometric HfN. The experimental results are supported by ab-initio calculations showing a high propensity of HfN_y to form cation vacancies and interstitial nitrogen and support the agglomeration of existing defects. Micropillar compression tests of sculptured $HfN_{1.22}$ pillars reveal metal-like global plastic deformation with activation of multiple {111}<110> slip-systems and large strain hardening due to dislocation interactions. Concurrently the films exhibit a high hardness. The noteworthy room-temperature ductility is facilitated by a high intrinsic dislocation density from growth, including mobile dislocation loops and facile dislocation nucleation enabled by the checkerboard superstructure. An improved toughness is shown by effective crack-arrest. Such durable hard coating properties present a long sought-for improvement for applications in tough environments, and we believe that this innovative nanoscale superstructuring can be applied to various nitride and carbide ceramics for coating applications.

Methods

Growth and Composition

The films were grown by reactive DC magnetron sputtering in a high-vacuum chamber having background pressure lower than 6.4×10^{-4} Pa. A $d = 75$ mm (3") elemental Hf-target (99%) in coupled unbalanced type II magnetron configuration was used to sputter in Ar + N_2 gas mixture at 0.6 Pa with a N_2 partial pressure of 0.067 Pa at 800 °C. The MgO(001) substrates were cleaned and pre-annealed (900 °C for 1 h) before deposition using the procedure outlined in[55]: sonication in detergent (2 vol%), de-ionized water, acetone and ethanol respectively.

Table 2 | Deposition parameters, film thickness, and ion assistance parameters

	$HfN_{1.22}$	$HfN_{1.33}$
Target power [W]	250	125
Deposition time [h]	2	2.5
Film thickness [μm]	2.5	0.9
Ion energy [eV]	24	22
Ion-to-metal flux ratio	15	28

High flux of low energy ion assistance was applied to the growing film using a −30 V substrate bias for improved magnetron sputter epitaxy. The target plasma was extended and directed to the substrate table using a solenoid around the substrate table, which coupled the magnetic field from the magnetron as explained elsewhere[56]. The ion-to-metal flux ratio, incident on the sample and the ion energy was calculated from results obtained by area (1 cm^2) and Langmuir (W-wire, $d = 0.5$ mm) plasma probes[57]. Deposition parameters and results of the two films are listed in Table 2. Both ion energy and ion-to-atom flux ratio can affect the film growth substantially[21–23], in particular for denser films and a layer-by-layer growth with a particular texture.

The chemical composition of the films was analyzed by a combination of Rutherford backscattering spectrometry (RBS) and time-of-flight elastic recoil detection analysis (ToF-ERDA), where the latter was used to quantify lighter elements. Both experiments were conducted at the tandem accelerator at Ångströmslaboratoriet, Uppsala University. As RBS and ToF-ERDA analysis require thin samples, ~200 nm thick films were deposited on Si(001) substrates at otherwise identical conditions. For RBS a 2 MeV $^4He^{2+}$ probe was incident at 5° to the sample normal and detector at a 170° scattering angle while the sample was continuously tilted in small random motions about 2° around the setpoint. Reference samples (Au, Cu, SiC, TiN) was used for analysis using SimNRA[58]. ToF-ERDA used a 36 MeV $^{127}I^{8+}$ probe incident at 22.5° to the sample surface and with a scattering angle of 45° to the detector. The ToF-energy histograms were analyzed using Potku software[59]. In combination, the composition error is estimated to be better than 0.03 for the metal/nitrogen ratio. The RBS simulation also provided surface density of the film which was used to calculate:

1. The mass density of the films by comparing with the film thickness.
2. The ion-to-metal flux ratio by combining the results of the plasma area probe and calculating the number of Hf atoms arriving on the substrate per second.

Structural characterization

X-ray diffraction (XRD) θ-2θ scans were acquired using a Panalytical X'Pert Pro powder diffractometer with monochromatic Cu-kα radiation in the Bragg-Brentano geometry. A divergence and acceptance slit of ½° were used. ω-scan rocking curves were acquired in a Panalytical Empyrian with high-resolution optics, hybrid Cu-Kα monochromator and 3-bounce Ge-crystal analyzer. Reciprocal space maps were used to evaluate the film quality, relaxed lattice parameter, a_0, limited lateral size, L, (lateral x-ray coherence length) and mosaic tilt. More details on calculations and analysis can be found in Supplementary Section 3. The maps were acquired in the same diffractometer using a hybrid monochromator, and an open 2D pixel detector was operated in scanning line mode for faster acquisition.

Cross-sectional transmission electron microscopy (TEM) samples of the as-grown films were prepared by a standard method where two cut pieces of the sample are sandwiched and glued face-to-face in a Ti-grid, mechanically polished until ~50 μm thickness and ion-milled until electron transparent using 5 keV Ar^+ at a 5° incidence angle, followed by 25 minutes of ion polishing at 1–1.9 keV. Atomic resolution high angle annular dark field scanning transmission electron microscopy (HAADF STEM) was performed in Linköping's double Cs corrected Titan^3 60-300 microscope, operated at 300 keV. Selected area electron diffraction (SAED) patterns were acquired in a FEI Tecnai G2 microscope operated at 200 keV.

Computational details

Kohn-Sham density-functional theory (DFT) calculations and ab initio molecular dynamics (AIMD) simulations were carried out using VASP[60], implemented with the projector augmented wave method[61] and the Perdew-Burke-Ernzerhof (PBE) approximation[62] to the electronic exchange and correlation energies. Among various local and semi-local functionals, the PBE approximation has been shown to be the most accurate at reproducing experimental values of monovacancy formation energies in elemental metals[63].

DFT calculations evaluate the formation energies of isolated point defects, small defect clusters, as well as the energies of defect distributions with stochastic and ordered arrangements. Metal vacancies, V_{Me}, nitrogen in antisite (cation) position, N_{AS}, and nitrogen self-interstitials, N_{SI}, were introduced into supercells comprised of 108 anion and 108 cation sites, corresponding to 3x3x3 conventional NaCl-structure unit cells. In AIMD, the composition of $HfN_{1.22}$ was mimicked by $Hf_{0.91}N_{1.10}$, in a supercell with 98 Hf and 119 N atoms.

DFT calculations of defect formation energies in nitrides require reference chemical potentials for nitrogen and metal species. We adopt N_2 gas molecules and hcp metals as done in previous DFT studies[29,30], To compute the energies of hcp metals, we employ 8-atom supercells with $12 \times 12 \times 12$ Monkhorst-Pack (MP)[64] **k**-point meshes and 500 eV cutoff energies. The N_2 dimer is placed in a cell with size of $15 \times 15 \times 15$ Å^3. The molecule's energy and the N ≡ N equilibrium distance are computed using a planewave cutoff of 700 eV.

To obtain DFT and AIMD predictions with equal level of accuracy, we perform all computations and simulations using $2 \times 2 \times 2$ MP sampling of the reciprocal space and 400 eV cutoff energies for the planewave basis set. These parameters yield a good balance between computational efficiency and accuracy. In DFT calculations, conjugate-gradient optimization of all structural degrees of freedom is reiterated to meet an energy accuracy of 10^{-5} eV/supercell and a force accuracy of 10^{-2} eV · Å^{-1}. In AIMD, forces on atoms are computed when the electron-density iterations reach an accuracy of 10^{-5} eV/supercell. The equations of motion are integrated on a time-step of 1 fs.

The identification of representative defect arrangements in Hf_yN_x is done with the aid of AIMD. AIMD simulations are assisted by on-the-fly training of a machine-learning interatomic potential (MLIP), as implemented in VASP 6.4.3. The flowchart in Supplementary Section 5 provides a schematic description of the procedure. Briefly: we construct $HfN_{1.22}$ supercells with lattice structure, chemical composition, and density that mimic the information collected by experimental characterization. AIMD simulations employ velocity-rescaling to control a cyclic annealing/cooling scheme between 300 and ≈2500 K. Annealing promotes diffusion and reorganization of point defects. The simulations follow the structural evolution during 0.2 ns. The structure obtained from the final cooling is fully relaxed by DFT at 0 K. As explained in the results and discussion section, our procedure leverages a representative defect configuration and outputs an MLIP able to describe accurately different Hf-N environments.

The energies of the defect structures in the supercell are computed by conjugate gradient relaxation using MLIP. Figure 3e shows that the energy of the configurations sampled via MC correlates well with a structural descriptor (D). The descriptor is defined as: $D = \text{std} \cdot \lambda$, where std is the standard deviation of the spatial distribution of cation vacancies, while λ is the sum of the distances of N self-interstitial defects from the average Cartesian coordinates of the vacancy cluster. Hence, the correlation shown in Fig. 3e indicates two structural conditions that tend to lower the defect energy in $Hf_{0.90}N_{1.10}$ (≡ $HfN_{1.22}$) supercells: (i) cation vacancies prefer to spread out over a relatively narrow volume and – at the same time – (ii) the N self-interstitial defects favor positions closer to the vacancy cluster.

Mechanical characterization

Nanoindentation using a Hysitron TI950 was used to measure film hardness. It was equipped with a Berkovich diamond tip with a radius of ~30 nm. Analysis was done according to the method by Oliver and Pharr[65]. 25 indents were measured for both samples at a load of 5 mN, resulting in an indentation depth of <90 nm, satisfying the 10% rule-of-thumb.

Cylindrical micropillars with a diameter of approximately 1 µm were milled on the $HfN_{1.22}$ film surface by focused ion beam (JEOL JEM-9320) system operated at 30 kV. An aspect ratio of ~2-3 was used (height/diameter). Compression tests were carried out in a load-controlled nanoindenter SHIMADZU DUH-211S equipped with a 20 µm flat-punch diamond tip at ambient temperature. An initial strain rate of all micropillars was controlled to approximately 10^{-2} s^{-1}. The pillars had a taper of ~4.5°, and the diameter for calculating the stress was taken as the average of the top and bottom diameters. The deformed micropillars were observed using a field-emission scanning electron microscope, JEOL JSM-7001FA. An electron transparent lamella of a representative compressed micropillar was prepared by conventional lift-out method using Carl Zeiss Crossbeam 1540 EsB focused ion beam/scanning electron microscopy workstation. Before thinning and lift out, an electron beam-induced Pt layer was deposited to provide protection from gallium implantation. For final thinning, a low-energy milling at 2 kV was performed to minimize Ga-induced damage.

An additional set of micropillars were tested from both $HfN_{1.22}$ and $HfN_{1.33}$ to verify the results presented in Fig. 4 and compare the two material compositions. Various $HfN_{1.22}$ pillar diameters were tested to evaluate the size effect: 810 nm, 640 nm, 480 nm and 300 nm. They were milled by a focused ion beam using a ThermoFisher Scios 2. The geometries were prepared using a Ga-ion probe current of 5 nA for the rough cut down to 50 pA for the finishing step. In-situ pillar compression was done in a Zeiss Sigma 500 VP system using FemtoTools FT-NMT04 in-situ SEM nanoindenter equipped with a 7 µm diameter flat diamond punch in a displacement-controlled mode with a displacement rate of 10 nm·s^{-1}. The pillars were loaded to different strains, up to a maximum of ~50% strain.

The correct alignment between the sample and tip was guaranteed by the following procedure: Before the actual loading of the pillar, indentation tests were carried out in the pristine coating, making sure that there was a sharp transition between the force recording in the vacuum and the loading of the film. Given that the angle between the two parts cannot be modified with this instrument, and the specimen must always be positioned the same way on the specimen holder due to the instrument's design, a one-time FIB alignment procedure was performed on the flat punch tip. The compressed pillars were imaged at a ~ 50° tilt angle by a Zeiss Sigma 300 scanning electron microscope using a 3 kV acceleration voltage and SE2 detector.

The load-displacement curves were converted into engineering stress-strain curves following an approach by Wheeler and Michler[66], where the top diameter of the pillar is taken as the reference contact area. The engineering strain was obtained from the displacement data using the pillar height and a corrected displacement data accounting for the base compliance following Sneddon's correction[67] given by:

$$\Delta L = \frac{1 - \upsilon_{sub}^2}{E_{sub}} * \frac{F}{d}$$

where ν_{Sub} and E_{Sub} are the biaxial Poisson's ratio and Young's modulus of the substrate, respectively, $\nu_{sub} = 0.18$, $E_{sub} = 291$ GPa[68]. F is the applied force, and d is the diameter of the pillars. ΔL is then the deformation of the substrate induced by the pillar and must be subtracted before calculating the strain.

The engineering stress-strain curves were further analyzed by binning the data in steps of 0.05 % strain. An average of the stress was calculated, a minimum of 3 pillars for each diameter was compressed to >30% strain except the pillars with 480 nm diameter, where a minimum of 3 tests was conducted up to ~23% strain. The minimum and maximum values of each set of pillars were taken as error bar. The strain hardening rate was calculated from the linear part of the flow stress from the average curves. The expected strain hardening rate was calculated by assuming a 2° taper and estimating the deformation region from SEM micrographs.

Data availability

All data used in this work is available on request. The datasets generated during the current study are available in the Zenodo repository, https://doi.org/10.5281/zenodo.14894490.

Code availability

All code used in this work is available upon request.

Received: 31 October 2024; Accepted: 3 March 2025;
Published online: 13 March 2025

References

1. Clegg, W. J. Controlling Cracks in Ceramics. *Science* **286**, 1097–1099 (1999).
2. Ritchie, R. O. The conflicts between strength and toughness. *Nat. Mater.* **10**, 817–822 (2011).
3. Evans, A. G. Perspective on the Development of High-Toughness Ceramics. *J. Am. Ceram. Soc.* **73**, 187–206 (1990).
4. Porz, L. et al. Dislocation-toughened ceramics. *Mater. Horiz.* **8**, 1528–1537 (2021).
5. Shen, C. et al. Achieving room temperature plasticity in brittle ceramics through elevated temperature preloading. *Sci. Adv.* **10**, eadj4079 (2024).
6. Dong, L. R. et al. Borrowed dislocations for ductility in ceramics. *Science* **385**, 422–427 (2024).
7. Mayrhofer, P. H., Clemens, H. & Fischer, F. D. Materials science-based guidelines to develop robust hard thin film materials. *Prog. Mater. Sci.* **146**, 101323 (2024).
8. Luo, Q., Lu, C., Liu, L. & Zhu, M. A review on the synthesis of transition metal nitride nanostructures and their energy related applications. *Green. Energy Environ.* **8**, 406–437 (2023).
9. Mayrhofer, P. H. et al. Self-organized nanostructures in the Ti–Al–N system. *Appl. Phys. Lett.* **83**, 2049–2051 (2003).
10. Sangiovanni, D. G., Hultman, L. & Chirita, V. Supertoughening in B1 transition metal nitride alloys by increased valence electron concentration. *Acta Materialia* **59**, 2121–2134 (2011).
11. Mei, A. B. et al. Adaptive hard and tough mechanical response in single-crystal B1 VNx ceramics via control of anion vacancies. *Acta Materialia* **192**, 78–88 (2020).
12. Kindlund, H. et al. Vacancy-induced toughening in hard single-crystal V0.5Mo0.5Nx/MgO(001) thin films. *Acta Materialia* **77**, 394–400 (2014).
13. Chen, Z. et al. Large mechanical properties enhancement in ceramics through vacancy-mediated unit cell disturbance *Nat. Commun.* **14**, https://doi.org/10.1038/s41467-023-57144060-x (2023).
14. Klimashin, F. F., Lobmaier, L., Koutná, N., Holec, D. & Mayrhofer, P. H. The MoN–TaN system: Role of vacancies in phase stability and mechanical properties. *Mater. Des.* **202**, 109568 (2021).
15. Fahrenholtz, W. G. & Hilmas, G. E. Ultra-high temperature ceramics: Materials for extreme environments. *Scr. Materialia* **129**, 94–99 (2017).
16. Buchinger, J. et al. Fracture properties of thin film TiN at elevated temperatures. *Mater. Des.* **194**, 108885 (2020).
17. Mei, A. B. et al. Physical properties of epitaxial ZrN/MgO(001) layers grown by reactive magnetron sputtering. *J. Vac. Sci. Technol. A Vac. Surf. Films* **31**, 061516 (2013).
18. Seo, H.-S., Lee, T.-Y., Petrov, I., Greene, J. E. & Gall, D. Epitaxial and polycrystalline HfNx (0.8⩽x⩽1.5) layers on MgO(001): Film growth and physical properties. *J. Appl. Phys.* **97**, 083521 (2005).
19. Johansson, B. O., Helmersson, U., Hibbs, M. K. & Sundgren, J. -E. Reactively magnetron sputtered Hf-N films. I. Composition and structure. *J. Appl. Phys.* **58**, 3104–3111 (1985).
20. Hu, C. et al. Negative effect of vacancies on cubic symmetry, hardness and conductivity in hafnium nitride films. *Scr. Materialia* **108**, 141–146 (2015).
21. Petrov, I., Barna, P. B., Hultman, L. & Greene, J. E. Microstructural evolution during film growth. *J. Vac. Sci. Technol. A* **21**, S117–S128 (2003).
22. Hultman, L., Helmersson, U., Barnett, S. A., Sundgren, J. -E. & Greene, J. E. Low-energy ion irradiation during film growth for reducing defect densities in epitaxial TiN(100) films deposited by reactive-magnetron sputtering. *J. Appl. Phys.* **61**, 552–555 (1987).
23. Petrov, I., Adibi, F., Greene, J. E., Hultman, L. & Sundgren, J. -E. Average energy deposited per atom: A universal parameter for describing ion-assisted film growth?. *Appl. Phys. Lett.* **63**, 36–38 (1993).
24. Powder diffraction file 00-025-1410 (HfN), reference code 00-033-0592. Natl. Bur. Stand. (U. S.) Monogr. 25, 19, 46, (1982).
25. Seo, H.-S. et al. Growth and physical properties of epitaxial HfN layers on MgO(001). *J. Appl. Phys.* **96**, 878–884 (2004).
26. Moram, M. A. & Vickers, M. E. X-ray diffraction of III-nitrides. *Rep. Prog. Phys.* **72**, 036502 (2009).
27. Schuller, I. K. New Class of Layered Materials. *Phys. Rev. Lett.* **44**, 1597–1600 (1980).
28. Lee, T. et al. Elastic constants of single-crystal TiN_x(001) ($0.67 \leq x \leq 1.0$) determined as a function of x by picosecond ultrasonic measurements. *Phys. Rev. B* **71**, 144106 (2005).
29. Gambino, D., Sangiovanni, D. G., Alling, B. & Abrikosov, I. A. Nonequilibrium ab initio molecular dynamics determination of Ti monovacancy migration rates in $B1$ TiN. *Phys. Rev. B* **96**, 104306 (2017).
30. Tsetseris, L., Kalfagiannis, N., Logothetidis, S. & Pantelides, S. T. Structure and interaction of point defects in transition-metal nitrides. *Phys. Rev. B* **76**, 224107 (2007).
31. Smirnova, E., Nourazar, M. & Korzhavyi, P. A. Internal structure of metal vacancies in cubic carbides. *Phys. Rev. B* **109**, L060103 (2024).
32. Wang, K. et al. A comparative study on the hardness, stress and surface free energy of HfN films grown by HIPIMS and direct-current magnetron sputtering. *Surf. Coat. Technol.* **477**, 130405 (2024).
33. Howe, B. et al. Growth and physical properties of epitaxial metastable Hf1−xAlxN alloys deposited on MgO(001) by ultrahigh vacuum reactive magnetron sputtering. *Surf. Coat. Technol.* **202**, 809–814 (2007).
34. Zauner, L. et al. Assessing the fracture and fatigue resistance of nanostructured thin films. *Acta Materialia* **239**, 118260 (2022).
35. Liu, S., Raghavan, R., Zeng, X. T., Michler, J. & Clegg, W. J. Compressive deformation and failure of CrAlN/Si3N4 nanocomposite coatings. *Appl. Phys. Lett.* **104**, 081919 (2014).
36. El Azhari, I. et al. Investigations on micro-mechanical properties of polycrystalline Ti(C,N) and Zr(C,N) coatings. *Acta Materialia* **149**, 364–376 (2018).
37. Dehm, G. et al. Can micro-compression testing provide stress–strain data for thin films?. *Thin Solid Films* **518**, 1517–1521 (2009). no. 5.
38. Aleman, A. et al. Unusual secondary slip activity at room temperature in VC single crystals. *Mater. Des.* **244**, 113195 (2024).
39. Kiani, S., Ratsch, C., Minor, A. M., Kodambaka, S. & Yang, J.-M. Orientation- and size-dependent room-temperature plasticity in ZrC crystals. *Philos. Mag.* **95**, 985–997 (2015).
40. Clarebrough, L. M. & Hargreaves, M. E. Work hardening of metals. *Prog. Met. Phys.* **8**, 1–103 (1959).
41. Vinson, K. Yu, X.-X., De Leon, N., Weinberger, C. R. & Thompson, G. B. Plasticity mechanisms in HfN at elevated and room temperature *Sci. Rep.*, **6**, https://doi.org/10.1038/srep34571 (2016).
42. Shan, Z. W., Mishra, R. K., Syed Asif, S. A., Warren, O. L. & Minor, A. M. Mechanical annealing and source-limited deformation in submicrometre-diameter Ni crystals. *Nat. Mater.* **7**, 115–119 (2008).
43. Uchic, M. D., Shade, P. A. & Dimiduk, D. M. Plasticity of Micrometer-Scale Single Crystals in Compression. *Annu. Rev. Mater. Res.* **39**, 361–386 (2009).
44. Salamania, J. et al. Elucidating dislocation core structures in titanium nitride through high-resolution imaging and atomistic simulations. *Mater. Des.* **224**, 111327 (2022).
45. Yu, H., Bahadori, M., Thompson, G. B. & Weinberger, C. R. Understanding dislocation slip in stoichiometric rocksalt transition metal carbides and nitrides. *J. Mater. Sci.* **52**, 6235–6248 (2017).
46. Kiani, S., Yang, J.-M. & Kodambaka, S. Nanomechanics of Refractory Transition-Metal Carbides: A Path to Discovering Plasticity in Hard Ceramics. *J. Am. Ceram. Soc.* **98**, 2313–2323 (2015).

47. Egeland, G. W. et al. Plastic deformation in zirconium nitride observed by nanoindentation and TEM. *J. Nucl. Mater.* **416**, 253–261 (2011).
48. Odén, M., Ljungcrantz, H. & Hultman, L. Characterization of the Induced Plastic Zone in a Single Crystal TiN(001) Film by Nanoindentation and Transmission Electron Microscopy. *J. Mater. Res.* **12**, 2134–2142 (1997).
49. Li, N. et al., Quantification of dislocation nucleation stress in TiN through high-resolution in situ indentation experiments and first principles calculations. *Sci. Rep.* **5**, https://doi.org/10.1038/srep15813 (2015),
50. Hultman, L., Shinn, M., Mirkarimi, P. B. & Barnett, S. A. Characterization of misfit dislocations in epitaxial (001)-oriented TiN, NbN, VN, and (Ti,Nb) N film heterostructures by transmission electron microscopy. *J. Cryst. Growth* **135**, 309–317 (1994).
51. Korte, S. & Clegg, W. J. Micropillar compression of ceramics at elevated temperatures. *Scr. Materialia* **60**, 807–810 (2009).
52. Wheeler, J. M., Raghavan, R., Chawla, V., Morstein, M. & Michler, J. Deformation of Hard Coatings at Elevated Temperatures. *Surf. Coat. Technol.* **254**, 382–387 (2014).
53. Liu, W., Liu, X., Zheng, W. T. & Jiang, Q. Surface energies of several ceramics with NaCl structure. *Surf. Sci.* **600**, 257–264 (2006).
54. Sangiovanni, D. G. et al. Descriptor for slip-induced crack blunting in refractory ceramics. *Phys. Rev. Mater.* **7**, 103601 (2023).
55. Le Febvrier, A., Jensen, J. & Eklund, P. Wet-cleaning of MgO(001): Modification of surface chemistry and effects on thin film growth investigated by x-ray photoelectron spectroscopy and time-of-flight secondary ion mass spectroscopy. *J. Vac. Sci. Technol. A* **35**, 021407 (2017).
56. Birch, J., Joelsson, T., Eriksson, F., Ghafoor, N. & Hultman, L. Single crystal CrN/ScN superlattice soft X-ray mirrors: Epitaxial growth, structure, and properties. *Thin Solid Films* **514**, 10–19 (2006).
57. Merlino, R. L. Understanding Langmuir probe current-voltage characteristics. *Am. J. Phys.* **75**, 1078–1085 (2007).
58. Mayer, M., Eckstein, W., Langhuth, H., Schiettekatte, F. & von Toussaint, U. Computer simulation of ion beam analysis: Possibilities and limitations. *Nucl. Instrum. Methods Phys. Res. Sect. B Beam Interact. Mater. At.* **269**, 3006–3013 (2011).
59. Arstila, K. et al. Potku – New analysis software for heavy ion elastic recoil detection analysis. *Nucl. Instrum. Methods Phys. Res. Sect. B Beam Interact. Mater. At.* **331**, 34–41 (2014).
60. Kresse, G. & Furthmüller, J. Efficient iterative schemes for ab initio total-energy calculations using a plane-wave basis set. *Phys. Rev. B* **54**, 11169–11186 (1996).
61. Blöchl, P. E. Projector augmented-wave method. *Phys. Rev. B* **50**, 17953–17979 (1994).
62. Perdew, J. P., Burke, K. & Ernzerhof, M. Generalized Gradient Approximation Made Simple. *Phys. Rev. Lett.* **77**, 3865–3868 (1996).
63. Glensk, A., Grabowski, B., Hickel, T. & Neugebauer, J. Breakdown of the Arrhenius Law in Describing Vacancy Formation Energies: The Importance of Local Anharmonicity Revealed by Ab initio Thermodynamics. *Phys. Rev. X* **4**, 011018 (2014).
64. Monkhorst, H. J. & Pack, J. D. Special points for Brillouin-zone integrations. *Phys. Rev. B* **13**, 5188–5192 (1976).
65. Oliver, W. C. & Pharr, G. M. Measurement of hardness and elastic modulus by instrumented indentation: Advances in understanding and refinements to methodology. *J. Mater. Res.* **19**, 3–20 (2004).
66. Wheeler, J. M. & Michler, J. Elevated temperature, nano-mechanical testing in situ in the scanning electron microscope. *Rev. Sci. Instrum.* **84**, 045103 (2013).
67. Sneddon, I. N. The relation between load and penetration in the axisymmetric boussinesq problem for a punch of arbitrary profile. *Int. J. Eng. Sci.* **3**, 47–57 (1965).
68. Zha, C.-S., Mao, H. & Hemley, R. J. Elasticity of MgO and a primary pressure scale to 55 GPa. *Proc. Natl Acad. Sci.* **97**, 13494–13499 (2000).

Acknowledgements

The authors gratefully acknowledge financial support from the Swedish Research Council, VR, 2018-05190_VR (N.G) and 2021-04426 (DGS), the Swedish Government Strategic Research Area in Materials Science on Advanced Functional Materials (AFM) at Linköping University (Faculty Grant SFO Mat LiU No. 2009 00971). Authors thanks MIRAI 2.0 seed-funding, connecting Swedish and Japanese universities, for collaboration initiation between Linköping and Nagoya university. L.H. acknowledges the Knut and Alice Wallenberg Foundation Scholar Grant KAW2019.0290. Ion beam analysis at Uppsala University, accelerator operation was supported by Swedish Research Council VR-RFI (Contract No. 2019-00191). DGS gratefully acknowledges financial support from the Competence Center Functional Nanoscale Materials (FunMat-II) (Vinnova Grant No. 2022-03071). Ab initio simulations were enabled by resources provided by the National Academic Infrastructure for Supercomputing in Sweden (NAISS) at the National Supercomputer Center (NSC) partially funded by the Swedish Research Council through grant agreement 2022-06725. The financial support (R.H.) by the Austrian Federal Ministry for Digital and Economic Affairs, the National Foundation for Research, Technology and Development, and the Christian Doppler Research Association is gratefully acknowledged (Christian Doppler Laboratory, Surface Engineering of High- performance Components).

Author contributions

M.L.: Project conception and design. Synthesized films and performed most of the experimental characterization, data interpretation and analysis. Wrote the original manuscript. Coordinated the co-author contributions in manuscript revisions. D.S.: Designed and performed the theoretical simulations and analysis. Revised the manuscript. Obtained research funding. N.T., T.Z. and R.H.: Micropillar fabrication, compression testing, and aided in data analysis of the compression experiments. Revised the manuscript. J.P.: TEM lamella fabrication of compressed pillars. Performed STEM imaging and aided in analysis. Revised the manuscript. L.H.: Contributed with data interpretation and analysis, supervision. Revised the manuscript. Obtained research funding. J.B.: Contributed with data interpretation and analysis, supervision. Revised the manuscript. Obtained research funding. N.G.: Project conception and design. Contributed with data interpretation and analysis, supervision. Revised the manuscript. Obtained research funding.

Funding

Open access funding provided by Linköping University.

Competing interests

The authors declare no competing interests.

Additional information

Supplementary information The online version contains supplementary material available at https://doi.org/10.1038/s43246-025-00768-5.

Correspondence and requests for materials should be addressed to Marcus Lorentzon or Naureen Ghafoor.

Peer review information *Communications Materials* thanks Paul Mayrhofer and the other, anonymous, reviewer(s) for their contribution to the peer review of this work. Primary Handling Editor: John Plummer. A peer review file is available.